Remote Sensing of Environment 344 (2026) 115524

Contents lists available at ScienceDirect

Remote Sensing of Environment

journal homepage: www.elsevier.com/locate/rse

Immediate remote sensing: Dynamic context-adaptive fusion for himawari-8/9 10-minute wildfire detection

Baomo Zhang, Qiang Zhang*, Zishuo Wang, Tongde Yang

Information Science and Technology College, Dalian Maritime University, Dalian, China

ARTICLE INFO

Edited by Dr Marie Weiss

Keywords:
Himawari-8/9
Wildfire detection
Immediate remote sensing
Adaptive fusion
Validation

ABSTRACT

Wildfires pose a serious threat to global ecosystems and human safety. Immediate remote sensing for wildfire detection using high-frequency geostationary satellites is crucial. To achieve this objective, this work proposes a novel Himawari-8/9 10-minute wildfire detection algorithm based on Dynamic Context-Adaptive Fusion (DCAF). The proposed method first introduces preprocessing to eliminate cloud interference. The core content abandons the traditional binary judgment logic, employing a sliding window to calculate local background statistics. A sigmoid function is used to transform multidimensional spectral and temporal anomaly features into wildfire potential probabilities, which are then weighted and fused. Finally, a three-dimensional spatiotemporal consistency verification module is designed to eliminate outliers, by using the physical continuity of the fire and incorporating land cover data for post-processing. Experimental results show that the proposed algorithm significantly outperforms the JAXA L2 WLF products on 50 instance wildfire datasets, achieving an F1 score of over 0.85, particularly demonstrating a significant advantage in detecting early wildfire points. In cross-validation with the MODIS fire products, it also surpasses traditional thresholding algorithms for wildfire detection.

1. Introduction

In recent years, global warming has led to an increase in drought and high temperatures, resulting in a continuous rise in the frequency and scale of wildfires. Wildfires release large amounts of aerosols and particulate matter, which not only exacerbate air pollution but also pose a serious threat to infrastructure, ecosystems and public health (Moritz et al., 2014). Studies have shown that wildfires can significantly affect ecosystems such as forests, grasslands and farmlands, damage soil fertility and biodiversity, and affect regional climate and air quality (Chen et al., 2023; Zhang et al., 2026a).

High destructiveness of wildfires makes timely and accurate fire monitoring crucial for disaster response and management (Xie et al., 2018; Chowdhury and Hassan, 2015). Satellite remote sensing is widely used to effectively monitor and warn of wildfires. Sensors carried by polar orbit satellites, such as the Moderate-Resolution Imaging Spectroradiometer (MODIS) and Advanced Very High Resolution Radiometer (AVHRR), the the Visible Infrared Imaging Radiometer Suite (VIIRS), can provide global coverage and high spatial resolution (ranging from hundreds of meters to 1km) (Schroeder et al., 2014; Giglio et al., 2016; Wang et al., 2026). However, their observation frequency is low, often passing over the Earth only a few times a day, making it difficult to capture rapidly changing fire conditions (Maier et al., 2013; Xu and Wooster, 2023). In contrast, geostationary satellites (e.g., Himawari-8/9, GK-2A) operate at a speed synchronized with the Earth's rotation, allowing them to continuously lock onto East Asia and the Pacific region for observation. Himawari-8/9 is equipped with the Advanced Himawari Imager (AHI), which provides full-disk observations of the Earth from geostationary orbit every 10min, enabling high-frequency continuous observation (Chen et al., 2021; Ding et al., 2022). This near real-time observation advantage makes it unique in monitoring sudden events such as wildfires (Liu et al., 2023; Kennedy et al., 1994). It should be noted that geostationary satellites can only observe their coverage area, and their spatial resolution is limited.

In satellite-based fire detection methods, early research proposed traditional thresholding methods (Filizzola et al., 2016; Gong et al., 2021; Xu and Zhong, 2017) or contextual methods (Flasse and Ceccato, 1996; Giglio et al., 2003). The principle of thresholding is to set a threshold and use the difference in brightness temperature in different bands to detect wildfires (Liew, 2019; Parto et al., 2020). The principle of contextual methods is to find the difference in contextual information between fire pixels and surrounding background pixels to detect fire

* Corresponding author.
Email address: qzhang95@dlmu.edu.cn (Q. Zhang).

https://doi.org/10.1016/j.rse.2026.115524
Received 12 January 2026; Received in revised form 29 May 2026; Accepted 1 June 2026

(Yan et al., 2020). Laneve et al. (2006) applied a change detection method to compare the temperature change between two consecutive images with the expected temperature change caused by natural day-night cycles in order to detect fires. These methods usually require setting key thresholds based on statistical data (Wickramasinghe et al., 2016). In general, thresholding and spatial context methods are easy to implement; however, these methods often face difficulties in selecting appropriate thresholds and have significant limitations. In recent work, machine learning and deep learning methods have been widely used (Seydi et al., 2022; De Almeida Pereira et al., 2021; Zhang et al., 2024a, 2022, 2025a). For example, Zhang et al. (2023a) constructed a fire-labeled dataset based on VNP14IMG fire products and applied a random forest model using multi-band observations from Himawari-8 for fire detection. Zhang et al. (2023c) designed a spatial-temporal-spectral recurrent neural network for wildfire detection and achieved good results. Zheng et al. (2024) proposed a wildfire detection method based on Himawari-8 data and developed four feature input strategies, integrating spectral, spatial and temporal features, and combined them with a random forest model to achieve the best wildfire detection performance. Zhang et al. (2025c) used the Transformer model to fuse multi-class and multi-source information from Himawari-8/9 satellites to detect early wildfires. Zhang et al. (2024b) constructed a multi-scale spatiotemporal feature fusion model based on deep learning and used 10-minute resolution data from Himawari-8/9 for near real-time wildfire detection.

Despite the progress made, current remote sensing methods for wildfire detection still face several challenges. The relatively coarse spatial resolution of geostationary satellites makes it difficult to capture small-scale fires (Johnston et al., 2018; Chen et al., 2022b). Studies have shown that geostationary satellite fire products have a large number of false alarms and need to be corrected by combining them with ground data (Chen et al., 2022a). Classical geostationary satellite fire detection algorithms are mainly based on context analysis, which identifies thermal anomalies by calculating the difference in brightness temperature between the pixel to be detected and the surrounding background pixels (Chen et al., 2017). However, there are challenges such as threshold rigidity and sensitivity to noise. Although deep learning-based methods perform well on specific datasets (Hong et al., 2022, 2023; Zhang et al., 2026b, 2025b), there also exist problems such as imbalanced samples and insufficient interpretability.

To address the aforementioned issues and further enhance the practicality of geostationary satellites in wildfire detection, this paper proposes a dynamic context-adaptive fusion algorithm for immediate remote sensing, achieving near real-time wildfire detection on a 10-minute timescale. The main contributions are summarized below:

- **Dynamic Contextual Thresholding:** The algorithm considers whether a pixel is abnormally hot to be related to its immediate environment (spatial background) and historical state (temporal background). It dynamically generates multi-dimensional thresholds for each pixel, improving its adaptability to different surface types, seasons, and weather conditions.
- **Probabilistic Multi-Indicator Fusion:** This method transforms the four fire point characteristic indicators (temporal, spatial, spectral and absolute brightness temperature) at the time of a fire into potential scores within the [0, 1] interval, and then performs weighted fusion. This reduces misjudgments caused by noise from a single indicator.
- **Spatiotemporal Coherence Constraint:** True fire points are continuous in temporal and spatial dimensions. Other fire points may exist near or around an identified fire point. Therefore, this algorithm incorporates a validation module after the initial evaluation to assess the consistency of nearby fire point detection results, thereby reducing potential false alarms.

2. Data

2.1. Himawari-8/9 satellite data

The Himawari-8/9 satellites were launched from Japan on October 7, 2014 and November 2, 2016, respectively. They are the first third-generation geostationary meteorological satellites to carry the AHI, with an observation range of 60°S-60°N and 80°E-160°W. AHI can acquire full-disk data with a temporal resolution of 10min and a spatial resolution of 0.5 to 2 km (Bessho et al., 2016). This study mainly uses Himawari-8/9 L1 gridded data, which are standard products derived from the AHI. Experiments by Liu et al. (2026) demonstrate that the Himawari-8 and Himawari-9 satellites have high consistency. Therefore, this work does not consider their differences. It can be downloaded from JAXA (Japan Aerospace Exploration Agency) P-Tree system (ftp://ftp.ptree.jaxa.jp/jma/netcdf).

2.2. JAXA l2 WLF products

The JAXA Level 2 Wildfire products (JAXA L2 WLF products) are fire products released by the Japan Aerospace Exploration Agency. They have a spatial resolution of 2 km and a temporal resolution of 10min. Product information includes the latitude and longitude of suspected fire pixels, fire radiative power, and time. The JAXA L2 WLF products detect fire pixels using bands 7 and 14 of the AHI to calculate the normalized deviation of brightness temperature. Fire points are detected by comparing the brightness temperature of the target pixel with the brightness temperature of surrounding background pixels (11×11 grid). This study uses the JAXA L2 WLF products as comparative data to verify the accuracy of the proposed method. Since January 2020, JAXA has publicly released these near real-time fire products, which can be downloaded from the FTP server: ftp://ftp.ptree.jaxa.jp/pub/pub/himawari/l2/wlf.

2.3. MODIS fire products

MODIS is an important tool for fire monitoring. It mainly uses the mid-infrared band to identify fire points on the land surface and provides information such as the time, location, and intensity of related fires (Justice et al., 2002). MODIS has high spatial resolution and global coverage, so it has more reliable wildfire detection accuracy than Himawari-8/9. The results of validating MODIS active fire detection products using high spatial resolution reference data show relatively good performance (Schroeder et al., 2011). Therefore, in this work, we use MODIS fire products as reference data to verify the wildfire detection accuracy of the proposed method. Although these products may contain false alarms and may miss small or transient fires due to the relatively low observation frequency, the validation scenarios we select in this study are large fire cases without cloud cover, which are detected by MODIS with high confidence. MODIS fire products provide information on a daily basis with a spatial resolution of 1 km. In the past two decades, MODIS fire products have been widely used for forest fire detection and post-disaster assessment.

2.4. Land cover products

Since water bodies, bare land and other land types are almost impossible to burn, this study uses land cover products for post-processing to further remove false alarms. MCD12Q1 is a global land cover product jointly released by NASA and Boston University. It is generated based on MODIS sensor data carried on the Terra (MOD) and Aqua (MYD) satellites. The temporal resolution is annual and the spatial resolution is 500 m. To address the spatial resolution inconsistency between this product and the Himawari-8/9 data, it was downsampled to ensure a consistent spatial resolution of 2 km across all products and data. This product uses an improved supervised classification algorithm and multi-temporal spectral information to systematically classify land cover on the surface (Friedl et al., 2010). MCD12Q1 has become one of the

Table 1
Information of 50 example wildfire scenes and corresponding Himawari-8/9 satellite data.

No.	Code	Lat.	Lon.	Time	Land cover type	Burned area(ha)	**Source**
1	FS-01	49.52° N	123.06° E	May 02, 2017, 3:40	Savannas	11,500	H-8
2	FS-02	46.72° N	130.42° E	Apr 25, 2018, 5:10	Croplands	NA	H-8
3	FS-03	40.76° N	114.98° E	Nov 27, 2018, 16:40	Grasslands	NA	H-8
4	FS-04	28.20° N	101.44° E	Feb 10, 2019, 2:30	Grasslands	20	H-8
5	FS-05	36.40° N	112.32° E	Mar 14, 2019, 8:00	Croplands	667	H-8
6	FS-06	36.88° N	112.18° E	Mar 29, 2019, 5:10	Grasslands	942	H-8
7	FS-07	40.30° N	116.98° E	Mar 30, 2019, 5:40	Savannas	20	H-8
8	FS-08	27.16° N	101.44° E	Mar 30, 2019, 9:30	Woody Savannas	20	H-8
9	FS-09	41.92° N	123.64° E	Apr 17, 2019, 6:00	Grasslands	829	H-8
10	FS-10	37.30° N	121.56° E	Mar 17, 2020, 7:30	Croplands	60	H-8
11	FS-11	27.80° N	102.20° E	Mar 30, 2020, 8:10	Croplands	3048	H-8
12	FS-12	51.20° N	128.30° E	Apr 14, 2020, 3:10	Savannas	NA	H-8
13	FS-13	35.96° N	120.10° E	Apr 23, 2020, 6:10	Grasslands	1285	H-8
14	FS-14	27.98° N	100.56° E	Dec 28, 2020, 7:00	Evergreen Needleleaf Forest	106	H-8
15	FS-15	25.82° N	113.80° E	Jan 19, 2021, 5:00	Savannas	NA	H-8
16	FS-16	35.96° N	106.10° E	Mar 13, 2021, 4:30	Croplands	267	H-8
17	FS-17	25.16° N	102.74° E	Mar 14, 2021, 5:30	Urban and Built-up	68	H-8
18	FS-18	26.02° N	103.10° E	Mar 17, 2021, 7:30	Croplands	7	H-8
19	FS-19	25.72° N	102.40° E	Mar 29, 2021, 16:30	Evergreen Needleleaf Forest	53	H-8
20	FS-20	25.80° N	100.08° E	May 09, 2021, 4:50	Mixed Forest	48	H-8
21	FS-21	29.04° N	101.48° E	Feb 16, 2022, 6:40	Evergreen Needleleaf Forest	172	H-8
22	FS-22	26.06° N	102.60° E	Mar 10, 2022, 8:10	Savannas	42	H-8
23	FS-23	26.04° N	94.76° E	Mar 15, 2022, 4:10	Woody Savannas	NA	H-8
24	FS-24	27.18° N	99.76° E	Mar 15, 2022, 10:30	Evergreen Needleleaf Forest	1093	H-8
25	FS-25	41.98° N	123.78° E	Apr 23, 2022, 7:20	Grasslands	67	H-8
26	FS-26	25.52° N	110.46° E	Oct 17, 2022, 2:00	Savannas	NA	H-8
27	FS-27	27.78° N	102.34° E	Apr 10, 2023, 8:00	Evergreen Broadleaf Forest	3	H-9
28	FS-28	24.32° N	102.64° E	Apr 11, 2023, 7:20	Croplands	33	H-9
29	FS-29	25.46° N	100.46° E	Apr 17, 2023, 8:00	Woody Savannas	NA	H-9
30	FS-30	25.04° N	102.32° E	May 06, 2023, 8:00	Woody Savannas	11	H-9
31	FS-31	28.20° N	101.56° E	May 27, 2023, 7:40	Evergreen Needleleaf Forest	19	H-9
32	FS-32	27.68° N	104.04° E	Feb 18, 2024, 7:30	Woody Savannas	57	H-9
33	FS-33	27.28° N	105.34° E	Feb 18, 2024, 8:00	Savannas	59	H-9
34	FS-34	26.10° N	105.00° E	Feb 19, 2024, 7:30	Savannas	NA	H-9
35	FS-35	26.34° N	106.34° E	Feb 19, 2024, 12:40	Croplands	14	H-9
36	FS-36	26.32° N	106.62° E	Feb 19, 2024, 21:20	Cropland/Natural Mosaic	NA	H-9
37	FS-37	29.74° N	101.44° E	Mar 16, 2024, 8:40	Woody Savannas	25,000	H-9
38	FS-38	25.93° N	98.54° E	Mar 18, 2024, 3:30	Evergreen Needleleaf Forest	40	H-9
39	FS-39	35.20° N	102.68° E	Mar 21, 2024, 5:50	Grasslands	20	H-9
40	FS-40	26.02° N	99.96° E	Apr 06, 2024, 6:30	Woody Savannas	7	H-9
41	FS-41	41.62° N	123.80° E	Apr 07, 2024, 5:20	Croplands	2	H-9
42	FS-42	24.80° N	103.14° E	Apr 10, 2024, 7:30	Savannas	93	H-9
43	FS-43	24.68° N	102.50° E	Apr 12, 2024, 8:30	Savannas	NA	H-9
44	FS-44	25.22° N	103.58° E	Apr 13, 2024, 4:30	Woody Savannas	NA	H-9
45	FS-45	38.06° N	140.14° E	May 04, 2024, 6:40	Croplands	95	H-9
46	FS-46	36.04° N	112.16° E	Jun 12, 2024, 8:20	Mixed Forest	NA	H-9
47	FS-47	30.04° N	101.02° E	Dec 09, 2024, 7:20	Woody Savannas	NA	H-9
48	FS-48	32.32° N	104.94° E	Feb 05, 2025, 8:30	Deciduous Broadleaf Forest	NA	H-9
49	FS-49	39.04° N	141.78° E	Feb 26, 2025, 4:40	Mixed Forest	637	H-9
50	FS-50	35.28° N	127.80° E	Mar 21, 2025, 6:40	Deciduous Broadleaf Forest	48,000	H-9

Burned area: Data sourced from the internet, some of which uses approximate estimates.

most widely used land cover datasets in surface ecological monitoring and environmental research.

2.5. Verification scenarios

As shown in Table 1, the typical wildfire cases include 50 sudden forest fires that have attracted widespread public attention in recent years. Fig. 1 shows the geographical distribution of these fire cases on the map, with a relatively high concentration of cases in southwestern China. We obtained information on the location, time of occurrence, and burned area of these fires through online resources and news reports. The burned area can reveal the scale of a wildfire, but some events did not report the burned area, resulting in some missing data in Table 1. The accuracy of the information was verified using the brightness temperature of band 7, the brightness temperature difference between band 7 and band 14, and satellite true-color imagery. The land cover type of the corresponding location is determined by querying latitude and longitude information, which reveals the type of fire (agricultural fire or forest fire). These fires all caused severe economic losses and casualties. The experimental part of this study will be based on this dataset.

3. Methodology

3.1. Model overview

During forest wildfires, satellite observations often reveal numerous anomalies, such as an increased brightness temperature in band 7. Furthermore, due to the different radiative responses of bands 7 and 14, fire pixels exhibit a more significant increase in brightness temperature in band 7, which is highly sensitive to high-temperature anomalies. In contrast, band 14 exhibits a relatively smaller temperature increase. The differences in characteristics between the two bands can be utilized. Considering the variations in forest wildfires occurring in different seasons, regions, and weather conditions, for example—the normal brightness temperature in desert areas is higher in summer than in forests in winter—spatial features are introduced. At the beginning of a wildfire, the brightness temperature at that moment is higher than

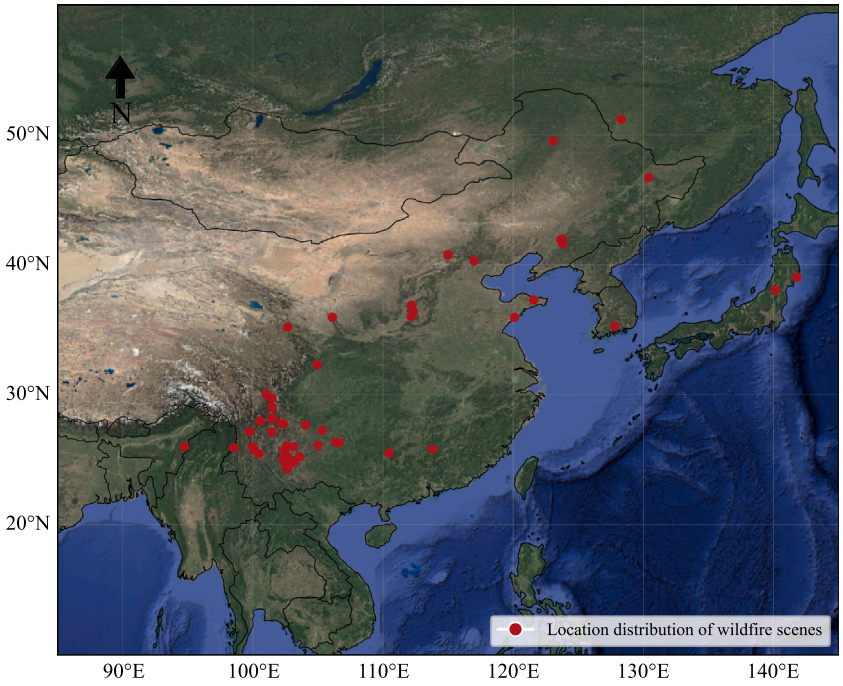

Fig. 1. Location distribution information for 50 typical wildfire scenarios.

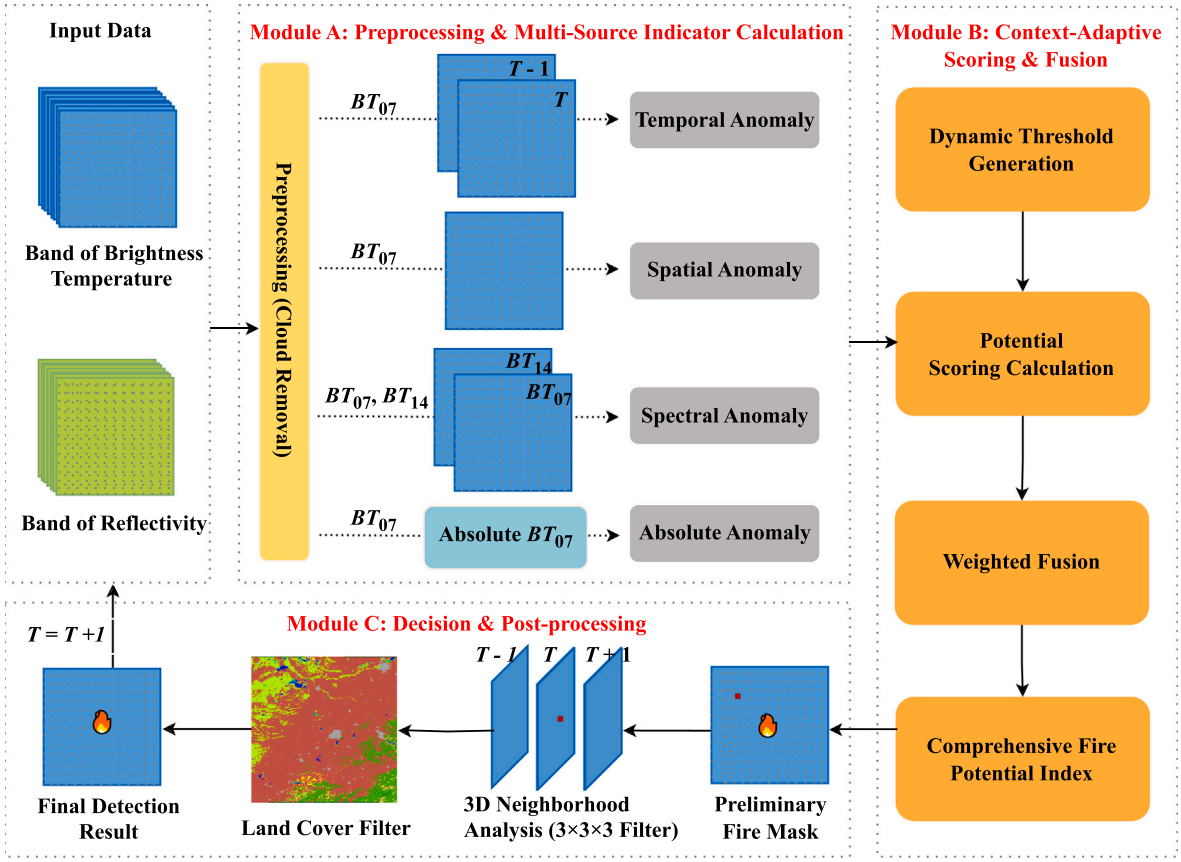

Fig. 2. Flowchart for building a fire detection model.

at the previous moment. Based on these characteristics of wildfire occurrences, this study proposes a dynamic context-adaptive fusion and spatiotemporal consistency verification algorithm, the overall flowchart of which is shown in Fig. 2. The core idea of this algorithm is to dynamically adjust the judgment criteria based on the background environment surrounding each pixel instead of using a fixed global threshold, and to

Table 2
Confusion matrix of predicted/actual fire or non-fire.

	Predicted Fire	Predicted Non-Fire
Actual Fire	TP	FN
Actual Non-Fire	FP	TN

fuse multiple fire point indicators into a continuous fire point potential value. Finally, spatiotemporal consistency is used to eliminate isolated false positives.

As shown in Fig. 2, spectral features are calculated based on the difference between bands 7 and 14. Temporal features are obtained by measuring the brightness temperature of fire pixels in band 7 at different times. Spatial features are obtained by calculating the variance between the target pixel and the background window. These data are then smoothly mapped to a dynamic threshold, weighted, and summed to determine the fire location. This method introduces a weighting mechanism to assign weights to various feature information to achieve effective and robust early wildfire detection. Furthermore, we consider heterogeneous information from land cover products to eliminate the influence of non-combustible surfaces.

3.2. Preprocessing and multi-source indicator calculation

3.2.1. Preprocessing

To handle cloud pixels, we use a thresholding method to create cloud masks (Zhang et al., 2023b). Cloud pixels are then excluded from subsequent fire detection, which eliminates false alarms caused by cloud cover and enhances the accuracy of wildfire detection. During the day, cloud pixels are defined as follows:

$$BT_{15} < 265\ \text{K and } R_3 + R_4 > 1.2 \text{ or } \left(\left(R_3 + R_4 > 0.7\right) \text{ and } \left(BT_{15} < 285\ \text{K}\right)\right) \tag{1}$$

At night, cloud pixels are defined as follows:

$$BT_{15} < 265\ \text{K and } BT_{07} < 285\ \text{K} \tag{2}$$

where R_3 and R_4 are the reflectivity data from bands 3 and 4 of the Himawari-8/9 satellite; BT_{07} and BT_{15} are the brightness temperature data from bands 7 and 15 of the Himawari-8/9 satellite.

3.2.2. Multi-source indicator calculation

Assuming the input brightness temperature data for band 7 is $BT_{07}(i,j,t)$ and band 14 is $BT_{14}(i,j,t)$, where i and j are the spatial coordinates and t is the time index. For each pixel in the central region (i,j) and for each time slice t, calculate the following four basic metrics:

Temporal Anomaly: The difference in brightness temperature compared to the previous moment:

$$I_1(i,j,t) = BT_{07}(i,j,t) - BT_{07}(i,j,t-1) \tag{3}$$

Spatial Anomaly: Referring to the research of Zhang et al. (2023c) and the detection methods of JAXA fire products, this study selected a 15×15 background window. Z-Score of the mean and standard deviation of the background brightness temperature of the target pixel and its surrounding 15×15 neighborhood (excluding itself):

$$I_2(i,j,t) = \frac{BT_{07}(i,j,t) - \mu_{bg}(i,j,t)}{\sigma_{bg}(i,j,t)} \tag{4}$$

where the background mean $\mu_{bg}(i,j,t)$ is calculated as the mean BT_{07} of all pixels within a 15×15 window centered on (i,j). The background standard deviation $\sigma_{bg}(i,j,t)$ is calculated as the standard deviation within this window of BT_{07}.

Table 3
Quantitative evaluation results of the DCAF and JAXA L2 WLF products across 50 current wildfire scenarios.

	JAXA L2 WLF					DCAF				
Code	EFA	FAR	OFR	F1	OA	EFA	FAR	OFR	F1	**OA**
FS-01	0.00	0.00	1.00	0.00	0.9578	1.00	0.00	0.16	0.91	0.9933
FS-02	0.00	0.00	0.91	0.17	0.9852	1.00	0.00	0.27	0.84	0.9960
FS-03	0.00	0.36	0.26	0.69	0.9911	1.00	0.16	0.00	0.92	0.9975
FS-04	0.00	0.00	0.92	0.15	0.9837	1.00	0.06	0.14	0.90	0.9965
FS-05	1.00	0.00	0.28	0.84	0.9916	1.00	0.00	0.12	0.94	0.9964
FS-06	0.50	0.00	0.25	0.86	0.9889	1.00	0.00	0.19	0.89	0.9916
FS-07	0.00	0.00	0.87	0.24	0.9956	1.00	0.42	0.07	0.72	0.9962
FS-08	0.00	0.00	1.00	0.00	0.9921	1.00	0.00	0.38	0.77	0.9970
FS-09	0.00	0.00	0.54	0.63	0.9747	1.00	0.00	0.20	0.89	0.9907
FS-10	0.00	0.19	0.19	0.81	0.9952	1.00	0.00	0.22	0.89	0.9973
FS-11	0.00	0.06	0.27	0.82	0.9969	1.00	0.06	0.30	0.81	0.9967
FS-12	0.00	0.65	0.49	0.42	0.9610	1.00	0.32	0.00	0.81	0.9872
FS-13	0.00	0.00	0.32	0.81	0.9938	0.33	0.00	0.36	0.78	0.9929
FS-14	0.50	0.37	0.20	0.70	0.9695	0.50	0.08	0.18	0.87	0.9886
FS-15	1.00	0.00	0.00	1.00	1.0000	1.00	0.00	0.00	1.00	1.0000
FS-16	0.50	0.00	0.50	0.67	0.9960	1.00	0.00	0.33	0.80	0.9973
FS-17	1.00	0.00	0.12	0.94	0.9987	1.00	0.07	0.00	0.96	0.9991
FS-18	0.00	0.00	0.67	0.50	0.9951	1.00	0.08	0.27	0.82	0.9975
FS-19	0.67	0.00	0.19	0.90	0.9960	1.00	0.02	0.00	0.99	0.9996
FS-20	0.00	0.00	1.00	0.00	0.9867	1.00	0.06	0.29	0.81	0.9956
FS-21	0.67	0.00	0.26	0.85	0.9964	1.00	0.08	0.00	0.95	0.9987
FS-22	0.50	0.12	0.32	0.77	0.9814	1.00	0.02	0.32	0.80	0.9849
FS-23	0.83	0.00	0.26	0.85	0.9944	1.00	0.00	0.26	0.85	0.9944
FS-24	1.00	0.49	0.34	0.58	0.9659	1.00	0.14	0.30	0.78	0.9857
FS-25	1.00	0.00	0.44	0.72	0.9911	1.00	0.24	0.09	0.83	0.9924
FS-26	0.25	0.22	0.09	0.84	0.9853	1.00	0.15	0.18	0.84	0.9862
FS-27	0.80	0.18	0.07	0.88	0.9941	1.00	0.00	0.20	0.89	0.9956
FS-28	0.14	0.00	0.38	0.77	0.9927	0.86	0.04	0.19	0.87	0.9956
FS-29	0.33	0.07	0.46	0.69	0.9886	1.00	0.01	0.19	0.89	0.9954
FS-30	0.00	0.00	0.60	0.57	0.9909	1.00	0.13	0.29	0.78	0.9940
FS-31	0.00	0.00	0.95	0.10	0.9900	1.00	0.41	0.11	0.71	0.9922
FS-32	0.50	0.00	0.61	0.56	0.9894	0.67	0.19	0.29	0.76	0.9922
FS-33	1.00	0.00	0.44	0.72	0.9879	1.00	0.07	0.14	0.89	0.9943
FS-34	0.27	0.00	0.56	0.61	0.9804	0.64	0.00	0.39	0.76	0.9867
FS-35	0.67	0.00	0.30	0.83	0.9952	1.00	0.00	0.19	0.89	0.9969
FS-36	0.00	0.20	0.20	0.80	0.9949	1.00	0.26	0.00	0.85	0.9956
FS-37	0.40	0.00	0.99	0.02	0.9303	1.00	0.00	0.19	0.89	0.9969
FS-38	0.00	0.00	0.95	0.10	0.9459	1.00	0.19	0.05	0.87	0.9930
FS-39	0.00	0.00	0.76	0.39	0.9935	0.67	0.00	0.36	0.78	0.9969
FS-40	0.00	0.00	0.95	0.09	0.9719	1.00	0.37	0.25	0.69	0.9798
FS-41	1.00	0.24	0.16	0.80	0.9949	1.00	0.39	0.00	0.76	0.9924
FS-42	0.00	0.00	0.55	0.63	0.9959	1.00	0.00	0.27	0.84	0.9979
FS-43	0.00	0.00	0.52	0.65	0.9915	1.00	0.48	0.13	0.66	0.9850
FS-44	0.56	0.02	0.43	0.72	0.9906	1.00	0.00	0.09	0.95	0.9981
FS-45	0.33	0.00	0.44	0.72	0.9928	1.00	0.00	0.29	0.83	0.9952
FS-46	0.00	0.00	0.74	0.42	0.9754	0.63	0.03	0.37	0.77	0.9870
FS-47	0.00	0.21	0.13	0.83	0.9884	1.00	0.00	0.00	1.00	1.0000
FS-48	1.00	0.00	0.92	0.16	0.9808	1.00	0.00	0.21	0.88	0.9956
FS-49	0.67	0.07	0.64	0.52	0.9741	1.00	0.08	0.21	0.85	0.9891
FS-50	1.00	0.10	0.24	0.82	0.9911	1.00	0.04	0.16	0.89	0.9946
Average	0.36	**0.07**	0.49	0.58	0.9857	**0.95**	0.09	**0.18**	**0.85**	**0.9938**

Spectral Anomaly: Difference in brightness temperature between bands 7 and 14:

$$I_3(i,j,t) = BT_{07}(i,j,t) - BT_{14}(i,j,t) \tag{5}$$

Absolute Anomaly: The brightness temperature of band 7:

$$I_4(i,j,t) = BT_{07}(i,j,t) \tag{6}$$

3.3. Context-adaptive scoring and fusion

Instead of directly applying fixed thresholds to the above indicators, we transform them into a potential score P_k between 0 and 1. The DCAF algorithm abandons the one-size-fits-all judgment and introduces the Sigmoid function, which is widely used in the fields of machine learning and pattern recognition for posterior probability modeling (Bishop,

2006). The Sigmoid function has smooth, continuous and monotonically increasing mathematical properties, and can nonlinearly map multidimensional real features such as absolute brightness temperature and spatial anomaly degree to the Fire Potential Probability in the (0,1) interval.

Temporal anomaly threshold: This indicator is already standardized. We set it to a small value that can reflect changes. In this paper, T_1 is set to 2.5K, indicating a rapid increase in temperature over a short period of time.

Spatial anomaly threshold: Similar to T_1, this metric has been standardized, and a relatively fixed threshold can be used, in this paper, it is set to 3.0K.

Spectral anomaly threshold: Defined as the mean plus the standard deviation within a $BT_{07} - BT_{14}$ range:

$$T_3 = \mu_{\Delta B,bg}(i,j,t) + n_3\sigma_{\Delta B,bg}(i,j,t) \tag{7}$$

where the background statistics $\mu_{\Delta B,bg}(i,j,t)$ and $\sigma_{\Delta B,bg}(i,j,t)$ represent the mean and standard deviation calculated from the neighborhood of $BT_{07} - BT_{14}$, respectively, n_3 is empirically set to 1.5.

Absolute BT threshold: Similarly,

$$T_4 = \mu_{bg}(i,j,t) + n_4\sigma_{bg}(i,j,t) \tag{8}$$

where the background statistics $\mu_{bg}(i,j,t)$ and $\sigma_{bg}(i,j,t)$ represent the mean and standard deviation calculated from the neighborhood of BT_{07}, respectively, n_4 is empirically set to 2.0, this is more flexible than the fixed threshold.

Regarding the four indicators I_k calculated above, their potential score is:

$$P_k(i,j,t) = \frac{1}{1+e^{-(I_k - T_k)}} \quad k = 1,2,3,4 \tag{9}$$

The four potential scores are weighted and summed to obtain the final Comprehensive Fire Potential Index:

$$S = \sum w_k p_k \quad k = 1,2,3,4 \tag{10}$$

where w_k represents the weights, and $\sum w_k = 1$. The weight settings reflect the importance of different indicators. Based on the physical characteristics of fire, spatial anomalies I_2 are usually the most critical indicators. The final weight allocation is: $w_1 = 0.3, w_2 = 0.3, w_3 = 0.15, w_4 = 0.25$. These weights can be trained and optimized using sample data.

3.4. Decision and post-processing

Set a final decision threshold T_{final}, this study uses a value of 0.5. If

$$S > T_{final} \tag{11}$$

the pixel (i,j,t) is initially identified as a fire point, it is identified as a non-fire point.

To further improve the detection results of forest wildfires, this study also employed post-processing. Post-processing aims to effectively eliminate false alarms of fire points in non-forested areas.

3.4.1. Spatiotemporal consistency check

To eliminate false positives, this method also verifies the initially identified fire points. For any initial fire point (i,j,t), its spatiotemporal continuity is checked. Spatially, it checks whether there are other initial fire points within its 8-neighborhood. Temporally, it checks whether there are any initial fire points within the pixel or its neighborhood at $T-1$ to $T+1$. Only when an initial fire point contains at least one other fire point within a 3×3×3 spatiotemporal cube is it confirmed as a final fire point. Isolated fire points will be discarded. The initial fire point is determined using a dynamic threshold. Spatio-temporal consistency checks are performed as a post-processing step. While this requires data from the next time step, false alarm removal may not be timely. However, considering the 10-minute resolution of the Himawari satellite, the impact is not significant.

3.5. Evaluation indicators

The following metrics were used to evaluate the wildfire detection performance in this study: Early Fire Accuracy (EFA), False Alarm Rate (FAR), Omission Fire Rate (OFR), F1 Score, and Overall Accuracy (OA). EFA primarily measures the model's accuracy in identifying fires in the early stages of a fire. A higher EFA indicates a higher proportion of early fire points being effectively identified, and better model performance in monitoring wildfires in their initial stages. Early detection of wildfires in their initial stages provides crucial support for early warning, fire rescue, and prevention deployment, thereby improving fire response efficiency and reducing disaster losses. FAR refers to the proportion of non-fire points incorrectly identified as fire points, while OFR represents the proportion of actual fire points that were not correctly identified by the model. The F1 score can be considered a comprehensive evaluation metric of model accuracy and recall, ranging from 0 to 1; a higher value indicates better overall model performance. OA reflects the model's overall ability to distinguish between fire points and non-fire points. However, it should be noted that when the background window is large and the time series is long, a high OA value may be due to a dominance of non-fire point samples and does not necessarily indicate excellent fire point detection capability. The specific calculations for each indicator are based on the confusion matrix of actual observations and model-predicted fire points shown in Table 2.

Based on the confusion matrix in Table 2, the calculation formulas of the above evaluation indicators are defined as follows:

$$\text{EFA} = \frac{EF_{\text{predict}}}{EF_{\text{all}}} \tag{12}$$

$$\text{FAR} = \frac{FP}{TP+FP} \tag{13}$$

$$\text{OFR} = \frac{FN}{TP+FN} \tag{14}$$

$$\text{F1-score} = \frac{2\times(1-FAR)\times(1-OFR)}{2-FAR-OFR} \tag{15}$$

$$\text{OA} = \frac{TP+TN}{TP+TN+FP+FN} \tag{16}$$

4. Experimental results

4.1. Testing results in instanced wildfire scenarios

As shown in Table 1, this study selected 50 wildfire scenarios as the validation dataset. These selected scenarios all garnered significant public attention and resulted in casualties. Table 1 details the spatial locations and temporal information of these 50 wildfire cases between 2017 and 2025. It also provides Himawari-8/9 satellite data corresponding to the early stages of the fires. All wildfire scenarios are identified using FS-n numbers, where n is the scenario number.

In the aforementioned 50 wildfire scenarios, the DCAF detection results were compared with the JAXA L2 WLF products. Table 3 presents the quantitative evaluation results for these 50 scenarios. The average test indicators are shown in Fig. 3. The F1 score of our method is 0.85, significantly higher than the 0.58 of the JAXA L2 WLF products; meanwhile, the FAR of our method is 0.18, lower than that of the JAXA products. Regarding the EFA indicator, the JAXA L2 WLF products only reached 0.36, repeatedly missing early fire points, while our method's EFA is 0.95, demonstrating its advantage in early wildfire detection. In terms of the false positive rate, the JAXA L2 WLF products are 0.07, while the proposed method is 0.09, seemingly performing better. However, this is due to fewer errors caused by too many missed

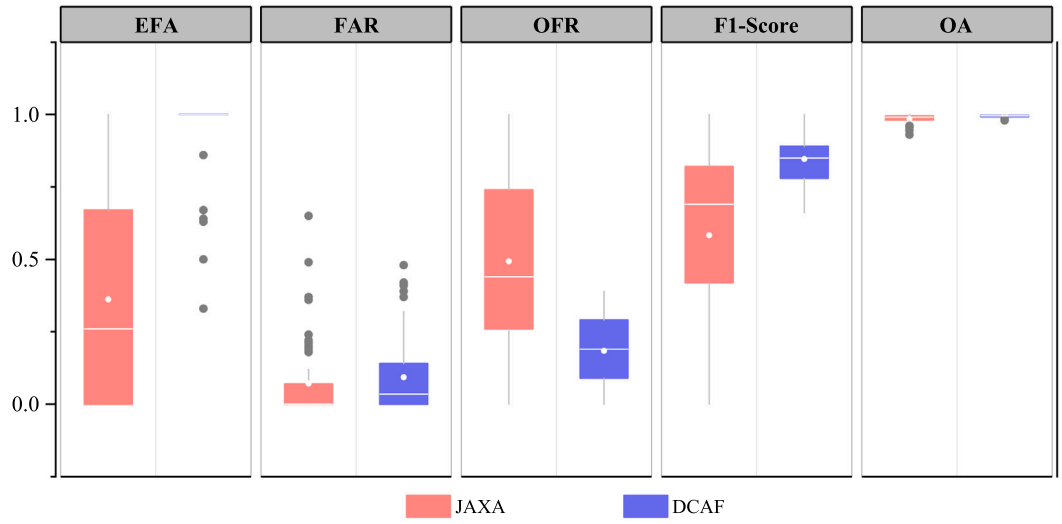

(a) Box plot of JAXA Wildfire products and DCAF evaluation metrics in 50 wildfire scenarios.

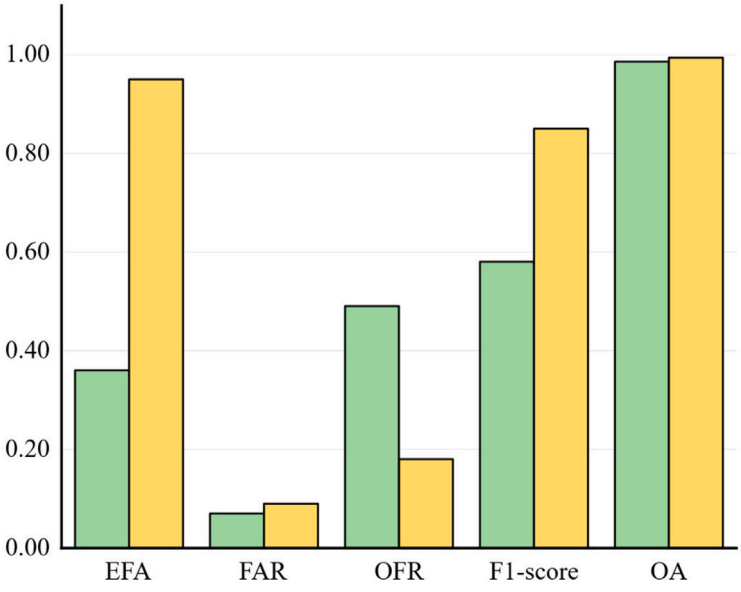

JAXA-mean	0.36	**0.07**	0.49	0.58	0.9857
DCAF-mean	**0.95**	0.09	**0.18**	**0.85**	**0.9938**

JAXA-mean DCAF-mean

(b) The average metrics of DCAF and JAXA L2 WLF products in 50 wildfire scenarios.

Fig. 3. Visual comparison of assessment metrics for 50 wildfire scenarios.

detections, as can also be seen from the F1 score. The bar chart in Fig. 3(b) more intuitively shows the comparison results in terms of mean values.

To more clearly illustrate the detection results of the two methods, Fig. 3 presents a visualization of the comparison between DCAF and JAXA L2 WLF products in 50 wildfire scenarios. Fig. 3(a) shows the box plots for each metric. The box plots show that DCAF outperforms JAXA in EFA, OFR, F1 score, and OA, reflected in its higher median, indicating improved detection accuracy and overall classification performance. Furthermore, DCAF exhibits narrower interquartile ranges on most metrics, indicating higher stability and robustness under various wildfire conditions. JAXA's results are more widely distributed and contain multiple outliers, suggesting greater sensitivity to scene changes. These results confirm that DCAF achieves a better balance between detection capability and false alarm control.

4.2. Large-scale study area

To investigate the applicability of the proposed method to a wider range, four representative forest fires and one large-scale agricultural straw burning incident in recent years were analyzed. The forest fires included three fires in Southwest China and one in South Korea, while the agricultural straw burning incident occurred in Northeast China. Southwest China, due to its high forest cover and monsoon climate

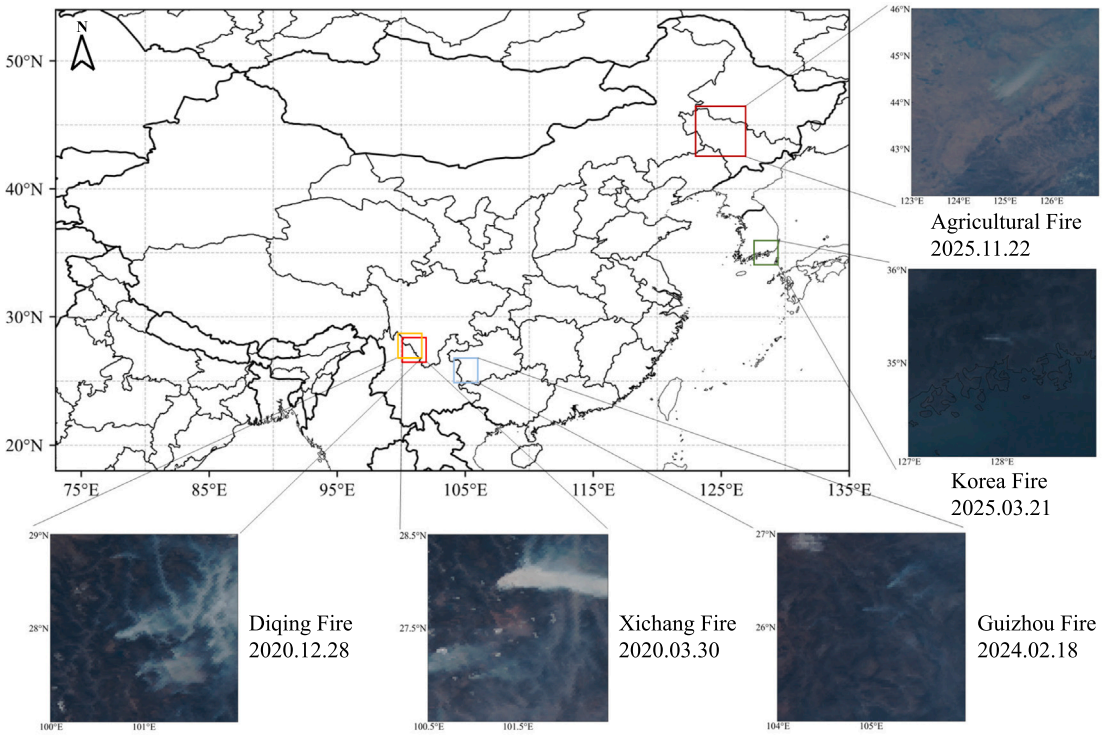

Fig. 4. Study areas of large-scale cross-validation.

with scarce rainfall during the dry season, experiences frequent forest fires. The burning of wasteland in Northeast China is rooted in its vast black soil belt and traditional agricultural land use practices, including marshes and wetlands. South Korea experienced its worst forest fire in history in early 2025 due to human factors. Detailed information on the five fire incidents is shown in Fig. 4.

4.3. Large-scale MODIS wildfire products cross-validation

4.3.1. Comparison algorithm

To better verify the effectiveness of the proposed method, we also selected two comparative methods to compare with the proposed method. (1) The algorithm proposed by Xu and Zhong (2017): the algorithm first uses bands 7 and 14 of Himawari-8 to identify potential fire points. Water masks (band 6) and cloud masks (bands 3, 4 and 15) are used to suppress false alarms of potential fire points. The low albedo of the visible light bands (bands 3, and 4) enables nighttime identification. This comparison algorithm is referred to as CA-1 in the following content. (2) The spatial context algorithm proposed by Giglio et al. (2003), which uses multiple context conditions to comprehensively judge fire points. This comparison algorithm is referred to as CA-2 in the following content.

4.3.2. Visualization results

To more intuitively demonstrate the advantages of the proposed method, this section presents an overlay analysis of the detection results for the wildfire scene in Fig. 4. Using the MODIS fire products as reference data, the detection performance of our method is compared with that of the JAXA L2 WLF products and two comparative algorithms. Due to the differences in temporal and spatial resolutions between the MODIS and AHI sensors, spatiotemporal matching processing is required before comparison. Fig. 5(a) shows the detection results of a wildfire in Sichuan Province on December 28, 2020, and Fig. 5(b) shows the true color image of Himawari-8. Due to the limitations of the MODIS product

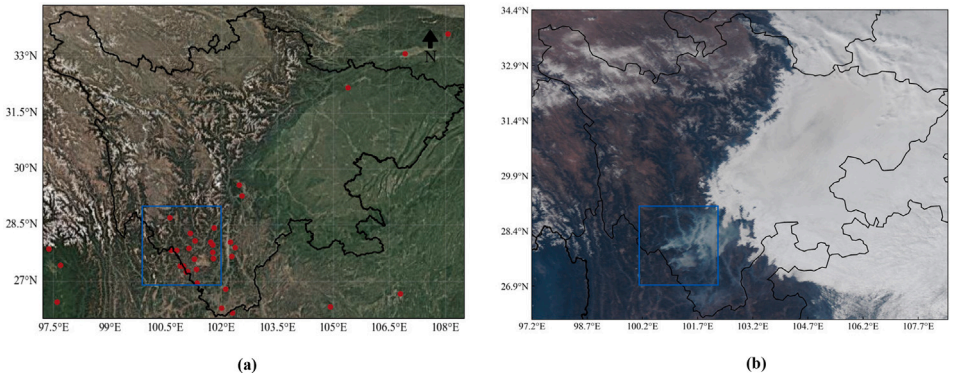

Fig. 5. (a) Detection results of a wildfire in Sichuan Province on December 28, 2020; (b) True-color image of Himawari-8. (For interpretation of the references to color in this figure legend, the reader is referred to the web version of this article.)

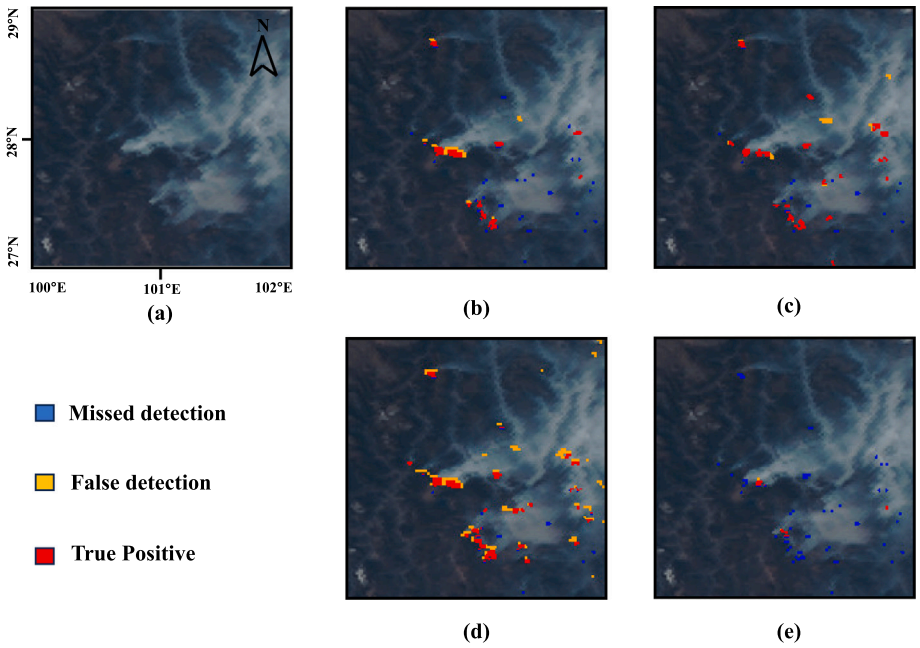

Fig. 6. Visual comparison of detection results for the Diqing wildfire: (a) true-color image; (b) JAXA L2 WLF products; (c) DCAF; (d) CA-1; (e) CA-2. (For interpretation of the references to color in this figure legend, the reader is referred to the web version of this article.)

transit time and the influence of cloud cover, our experiment only selected high-quality reference areas for detailed verification and analysis. In the visualization results, red dots represent detected fire points that overlap with the MODIS fire product results and are defined as true positives. Yellow and blue represent false positives and false negatives, respectively. The more red areas there are, the higher the consistency with the MODIS fire products.

Around 7:00 UTC on December 28, 2020, a forest fire broke out in Diqing Tibetan Autonomous Prefecture, Yunnan Province. Because Yunnan's vegetation is mainly coniferous forests such as pine, it easily forms difficult-to-control crown fires. At the time, the wind force at the fire site reached level 4, with gusts exceeding level 6 on the mountaintops, causing the fire to spread rapidly, as shown in the true-color image in Fig. 6(a). The scene is accompanied by multiple areas of dense smoke, indicating multiple fire lines. Fig. 6(c) shows the detection results of the proposed method. It can be seen from the figure that both the JAXA L2 WLF products and CA-2 have significant false negatives, while CA-1 detects relatively more fire points, but there

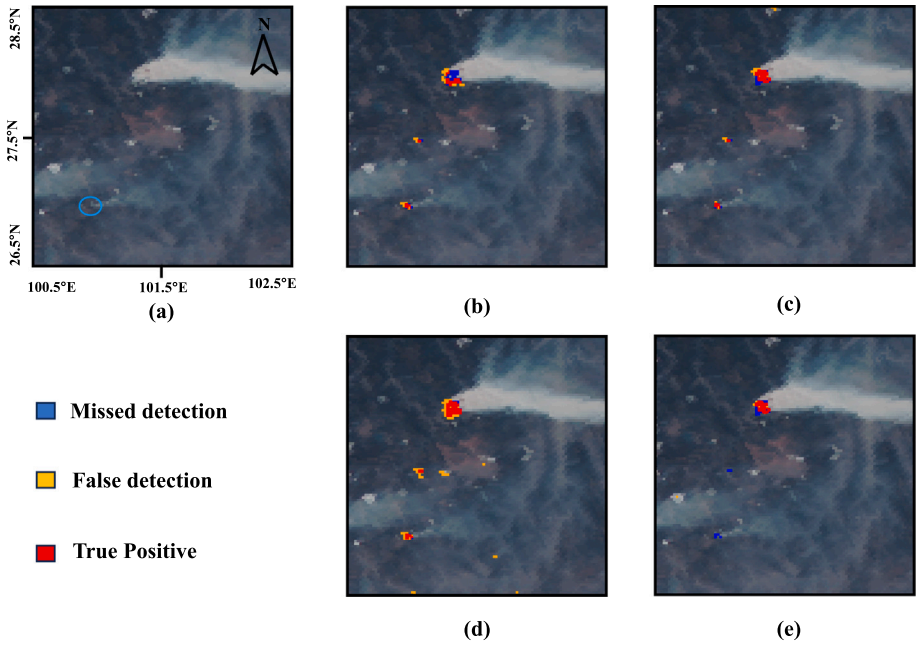

Fig. 7. Visual comparison of detection results for the Xichang wildfire: (a) true-color image; (b) JAXA L2 WLF products; (c) DCAF; (d) CA-1; (e) CA-2. (For interpretation of the references to color in this figure legend, the reader is referred to the web version of this article.)

are large yellow areas, indicating more false positives. In comparison, the proposed method shows higher consistency with the MODIS fire products.

Around 8:10 UTC on March 30, 2020, a forest fire broke out on the ridge of Pijia Mountain, at the border of Jingjiu Township and Anha Town, Xichang City, Liangshan Prefecture, Sichuan Province, China. The total burned area exceeded 3000 hectares. The investigation determined that the direct cause of the fire was a power line fault caused by a specific wind direction and force, which ignited the ground vegetation. Fig. 7(a) shows a Himawari-8 true-color image of the fire, with dense smoke clearly visible. In this scene, due to the large fire intensity, it can be seen from Fig. 7 that all four methods detected the fire points. However, in two smaller fire points, CA-1 and CA-2 showed false positives and false negatives.

To analyze the proposed method's ability to detect early fires, this study also performed a time-series analysis on a prominent fire point in Fig. 8, marked with a blue circle in Fig. 7(a). Fig. 8 shows the changes in brightness temperature of bands 7 and 14 over time, as well as the changes in their difference over time. It can be seen from the figures that the early fire occurred at approximately 3:10 UTC. Fig. 9 shows the detection results of the four methods. It can be seen that JAXA L2 WLF products and CA-2 both missed early fires, while CA-1 showed a serious false positive. The proposed method can quickly detect early wildfires with a low false positive rate.

Around 7:00 UTC on February 18, 2024, a wildfire broke out in Yachi Town, Qixingguan District, Bijie City, Guizhou Province. According to the official investigation, the cause of the fire was agricultural burning. In this case study, fire points with a confidence level greater than 70%

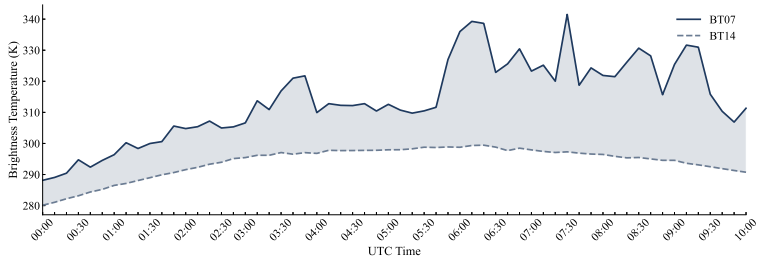

(a) Temporal analysis of brightness temperature in bands 7 and 14 of the fire point pixel.

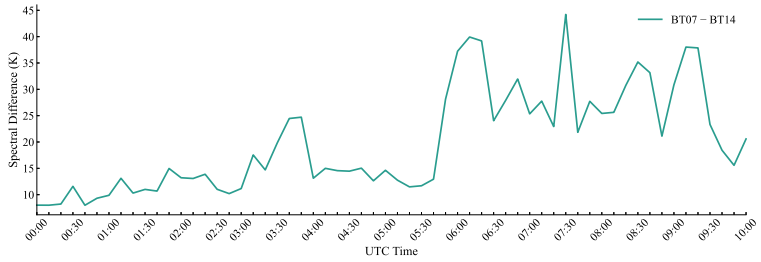

(b) Temporal analysis of brightness temperature in bands 7 minus bands14 of the fire point pixel.

Fig. 8. Temporal characteristics of brightness temperature at the fire point pixel.

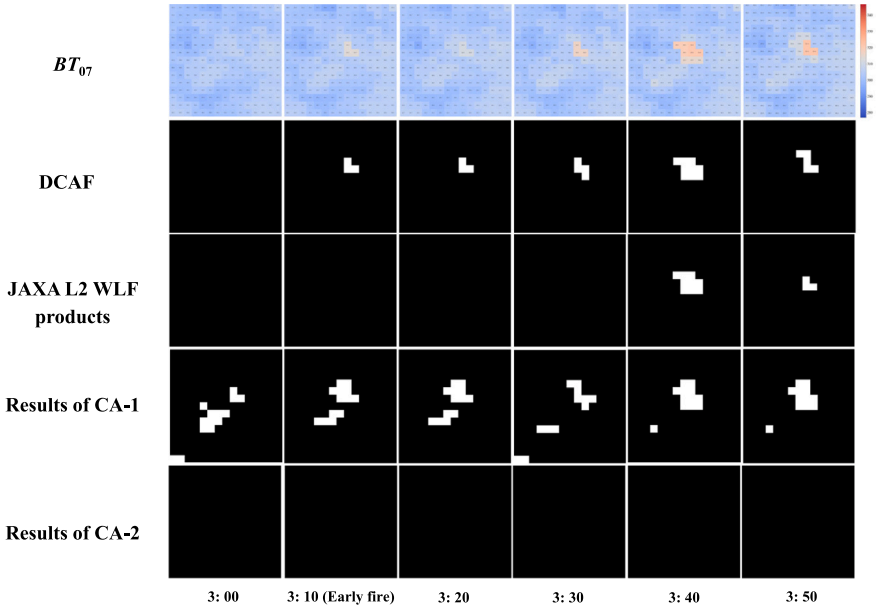

Fig. 9. Comparison of continuous detection at the same fire point using different methods.

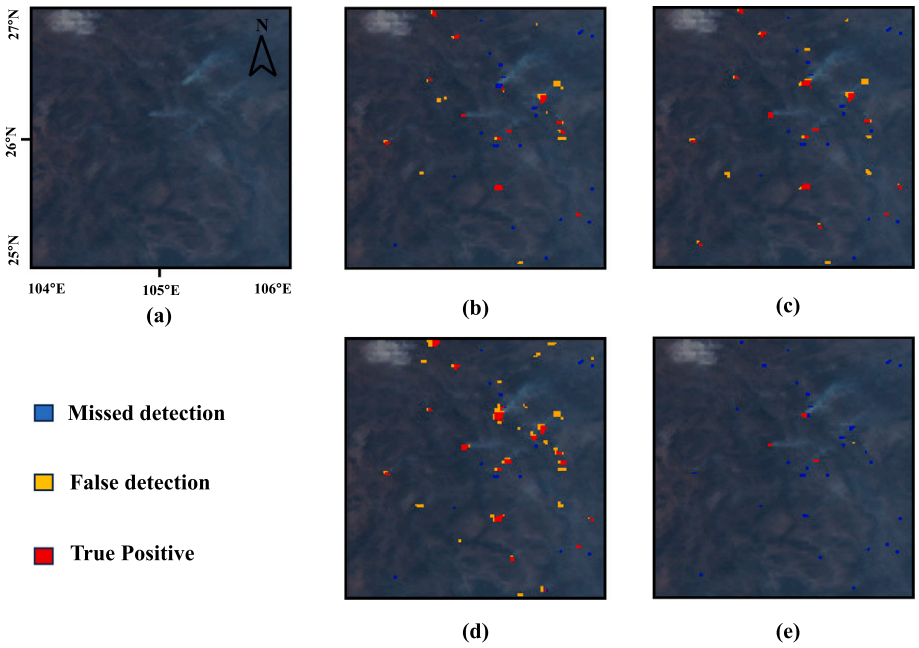

Fig. 10. Visual comparison of detection results for the Guizhou wildfire: (a) true-color image; (b) JAXA L2 WLF products; (c) DCAF; (d) CA-1; (e) CA-2. (For interpretation of the references to color in this figure legend, the reader is referred to the web version of this article.)

from the MODIS fire products were selected as a reference. Fig. 10(a) shows a Himawari-8 true-color image of the fire, with multiple smoke points indicating numerous fire spots. The figure also shows that CA-1 detected more fire points, but also had a high rate of false positives, while CA-2 had a high rate of false negatives. In comparison, the proposed method can balance the false positive rate and false negative rate, and has higher robustness.

MODIS fire products showed that fire points were concentrated during the wildfires in South Korea. Therefore, we conducted a long-term time-series analysis of this wildfire, as shown in Fig. 11. The brightness temperature map of band 7 indicates that the wildfire started around 6:40 UTC. The red box in the RGB image marks the location of the fire, and dense smoke is clearly visible. After the initial fire, both our proposed method and the JAXA L2 WLF products detected

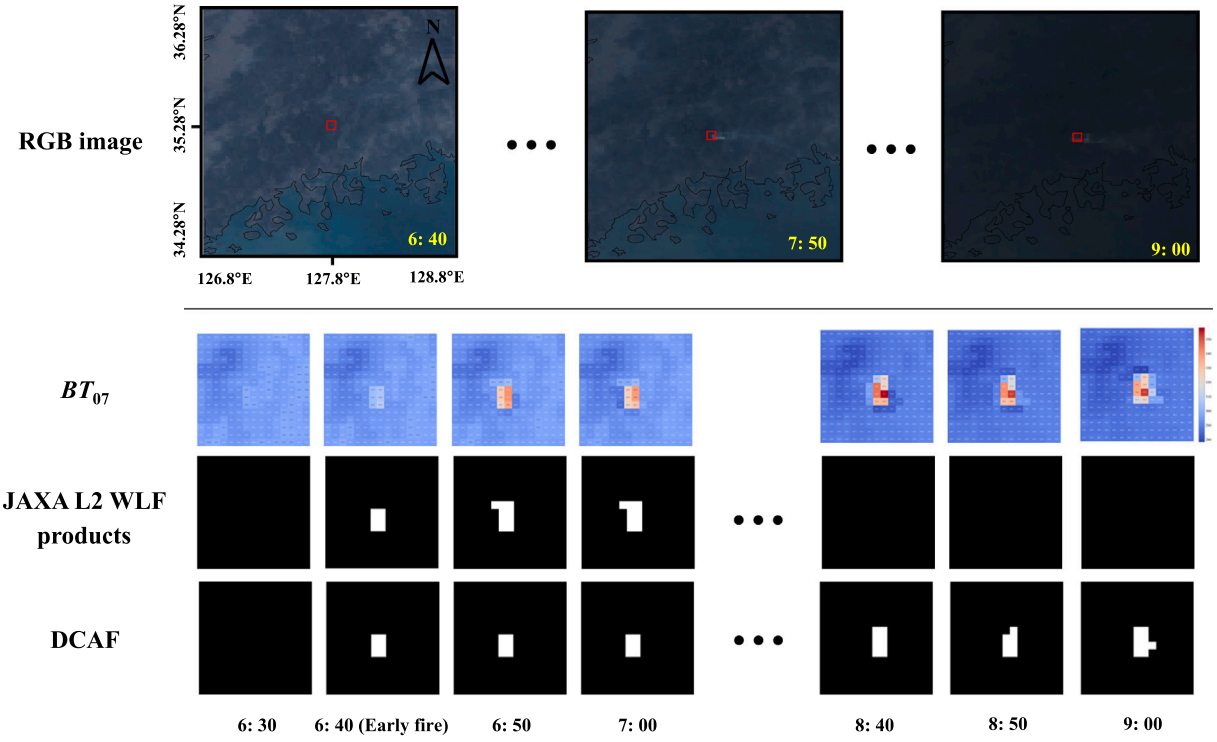

Fig. 11. Comparison of long-term monitoring data for the Korean wildfires.

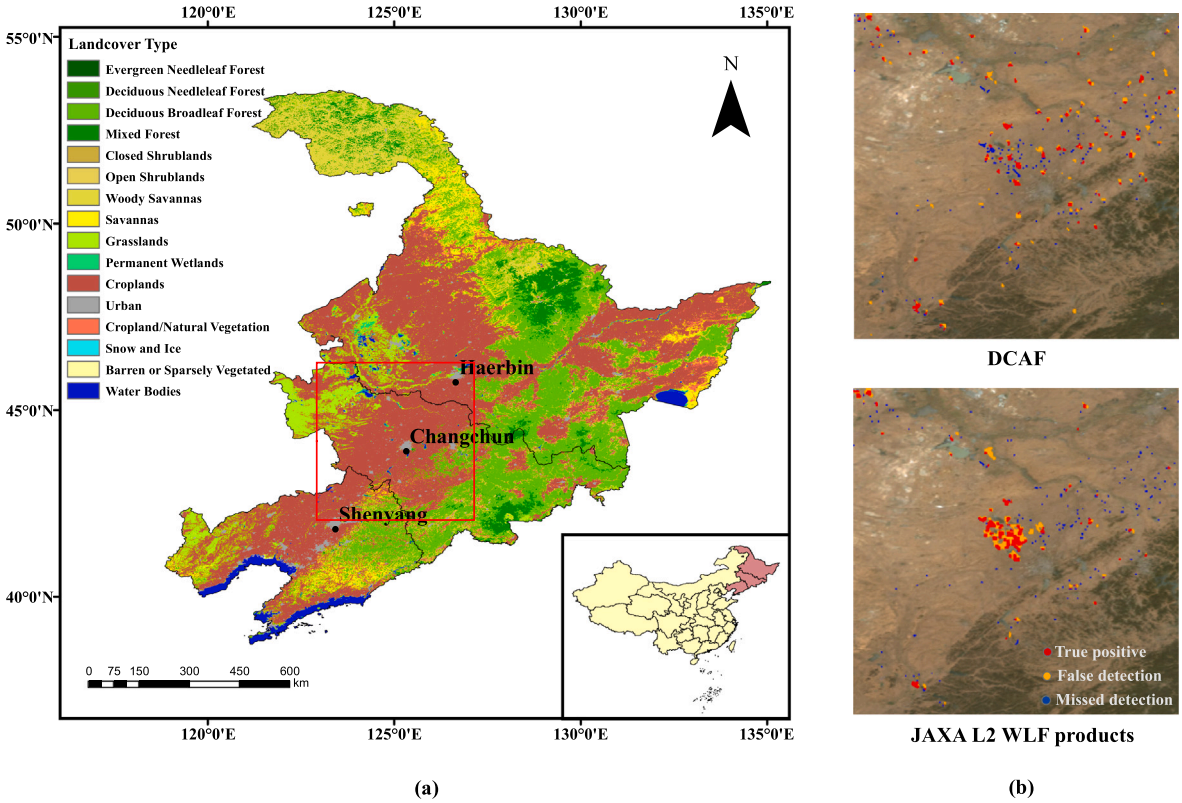

Fig. 12. (a) Schematic diagram of the land cover in Northeast China, with the red box corresponding to the area in figure (b); (b) detection results of the two methods. (For interpretation of the references to color in this figure legend, the reader is referred to the web version of this article.)

fire points around 8:40, about two hours later. The RGB image and brightness temperature map of band 7 show that the fire was still vigorous at this time; however, the JAXA L2 WLF products missed some detections. Our proposed method can maintain continuous fire detection.

Analysis of multiple fire case studies revealed that the JAXA L2 WLF products exhibited varying degrees of missed detections across different fire types. The CA-1 and CA-2 algorithms failed to balance the relationship between false positives and false negatives. In contrast, the method proposed in this study demonstrated stability in every case, successfully capturing the vast majority of fire points, thus validating its reliability in continuous fire detection.

4.4. Detection of agricultural fires

Northeast China is one of the regions with the most concentrated and abundant arable land resources in the country. Fig. 12(a) shows the land cover types of the three northeastern provinces. As can be seen from the figure, arable land accounts for a large part of the land types in Northeast China. Local people conduct concentrated burning in winter as a quick and economical means to clear straw, prevent pests and diseases, and improve soil fertility before spring plowing. In November 2025, large-scale burning occurred in Northeast China. Based on MODIS fire products and related news reports, we confirmed that large-scale burning occurred on November 22. This paper uses the proposed algorithm to detect this and compares it with the JAXA L2 WLF products, using the MODIS fire products as a reference. Because the burning range and intensity of agricultural fires are different from those of forest fires, they are usually scattered and less intense, making them more difficult to detect. Fig. 12(b) shows the detection results of the two methods. The proposed method can detect more discrete fire points in a large-scale background, while the JAXA L2 WLF products only detect many fire points in the central area of the selected region, and miss many discrete fire points.

5. Discussions

5.1. The rationale and regulation of burning stubble

The burning of wasteland in Northeast China is rooted in its vast black soil belt and traditional agricultural land use practices in marshland and wetlands. While it is a quick and economical means of clearing straw, controlling pests and diseases, and improving soil fertility before spring planting, it benefits agricultural production in the short term but has a significant negative impact on regional air quality. The large amounts of particulate matter (PM2.5, PM10), black carbon, and volatile organic compounds released during burning easily accumulate under relatively stable meteorological conditions in spring, forming regional smog. This not only reduces visibility but also affects downwind urban clusters through long-distance transmission, exacerbating the air pollution load across borders in the Beijing-Tianjin-Hebei region and even Northeast Asia. Furthermore, the toxic substances such as polycyclic aromatic hydrocarbons produced by the incomplete combustion of biomass increase public health risks. Fig. 13 shows a Sentinel-2 true-color image of wasteland burning in Northeast China on November 22, 2025. Therefore, large-scale, uncontrolled wasteland burning is unreasonable and should be strictly regulated.

Geostationary satellite monitoring systems are increasingly becoming a highly practical macro-level technological tool for monitoring and managing agricultural straw burning. Their core value lies in providing near real-time, wide-area, and continuous observation capabilities. Unlike polar orbit satellites, which only pass overhead once or twice

Fig. 13. Sentinel-2 true-color image of burning vegetation in Northeast China on November 22, 2025. (For interpretation of the references to color in this figure legend, the reader is referred to the web version of this article.)

a day, geostationary satellites can observe fixed areas at the minute level. This leap in temporal resolution makes it possible to capture short-lived, sudden fires like straw burning, effectively recording the onset, spread, and extinguishing of the fire, greatly overcoming the problem of missed reports caused by monitoring blind spots. In terms of practicality, it can construct an objective chain of regulatory evidence, transforming traditional human-intensive ground patrols into data-driven, precise positioning. This provides environmental protection departments with irrefutable satellite remote sensing evidence to pinpoint suspected illegal burning areas and trace responsible parties.

5.2. Discussion of algorithm limitations

The algorithm proposed in this study aims to solve the long-standing trade-off between false positives and false negatives in geostationary satellite fire detection. Due to the low spatial resolution of geostationary satellites, a fire may occupy only a small portion of a pixel. However, because band 7 has a strong radiative response to high-temperature sources, even sub-pixel-level fires may produce detectable thermal anomalies. The proposed DCAF algorithm enhances the detection of such anomalies by utilizing contextual comparisons with surrounding pixels, differences across different spectral bands, and the temporal continuity of geostationary satellite observations. These mechanisms in DCAF contribute to improving sensitivity to small or sub-pixel-level fires.

Despite its excellent performance, this method is still limited by the physical characteristics of the sensor and the algorithm's assumptions. The spatial resolution of the Himawari-8/9 mid-infrared band is 2 km. For small fire spots, if their burning area is too small, their radiant energy, after being averaged by large pixels, may not trigger background anomaly statistics, leading to false negatives. This is a common physical bottleneck in all current Earth satellite fire detection. The accuracy of cloud detection also affects the experimental results. In addition, regional sensitivity of parameters. The current weight allocation and parameters are based on empirical settings for general scenarios. In extreme surface environments, fixed parameters may require targeted fine-tuning or adaptive calibration.

5.2.1. The influence of clouds on the experiment

Although the algorithm can handle thin clouds and smoke interference, infrared radiation cannot penetrate dense cloud cover with extremely high optical thickness, rendering any algorithm based on the thermal infrared band ineffective, thus requiring cloud removal processing. In addition, dense smoke plumes from intense fires may occasionally exhibit cloud-like radiative characteristics, which could lead to potential misclassification. Fig. 14 illustrates the effectiveness of the cloud removal algorithm used in this experiment, and the false alarms that may occur without cloud masking. The cloud masking algorithm could effectively reduce false alarms caused by clouds. Future research will explore effective cloud detection using multispectral band combinations and deep learning methods.

5.3. Parameter sensitivity analysis

This study employs manual parameter settings based on physical experience. The selection of these parameters refers to the classic contextual fire detection algorithms and the physical properties of Wien's displacement law for band 7. This section will discuss the sensitivity of these parameters using the Xichang wildfire incident in March 2020 as an example. Using the F1 score as a reference, we fix the other parameters and vary one parameter within a reasonable range to evaluate its impact on the experimental results. The results are shown in Fig. 15, which illustrates the impact of changes in four thresholds and their weights on the F1 score. The thresholds used in this study are marked with dashed lines in the figure. It can be seen from the figure that the empirically set parameters generally remain near their optimal values. Among them, the spatial anomaly threshold has the greatest impact on the F1 score, while the spectral anomaly threshold has a relatively small impact. Regarding weights, since temporal anomalies have a significant impact on early wildfires, high weights lead to decreased detection performance, while a reasonable weight combination yields optimal performance.

Future research will strive to minimize the use of manual parameter settings and continue to explore optimal parameter combinations to achieve the best results.

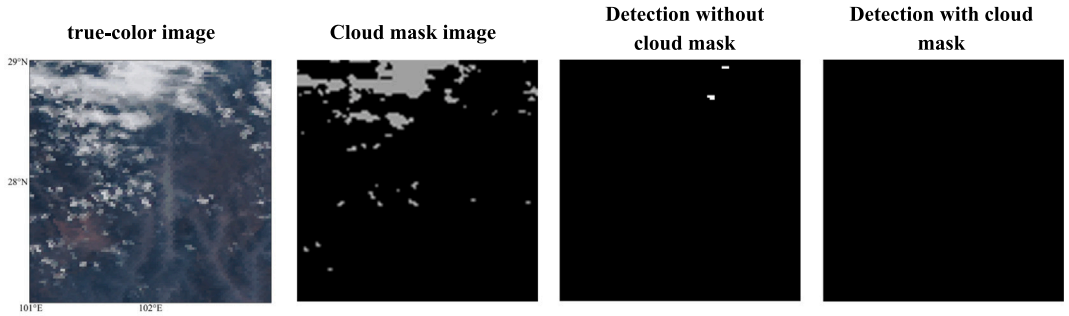

Fig. 14. The impact of the cloud masking algorithm in this experiment.

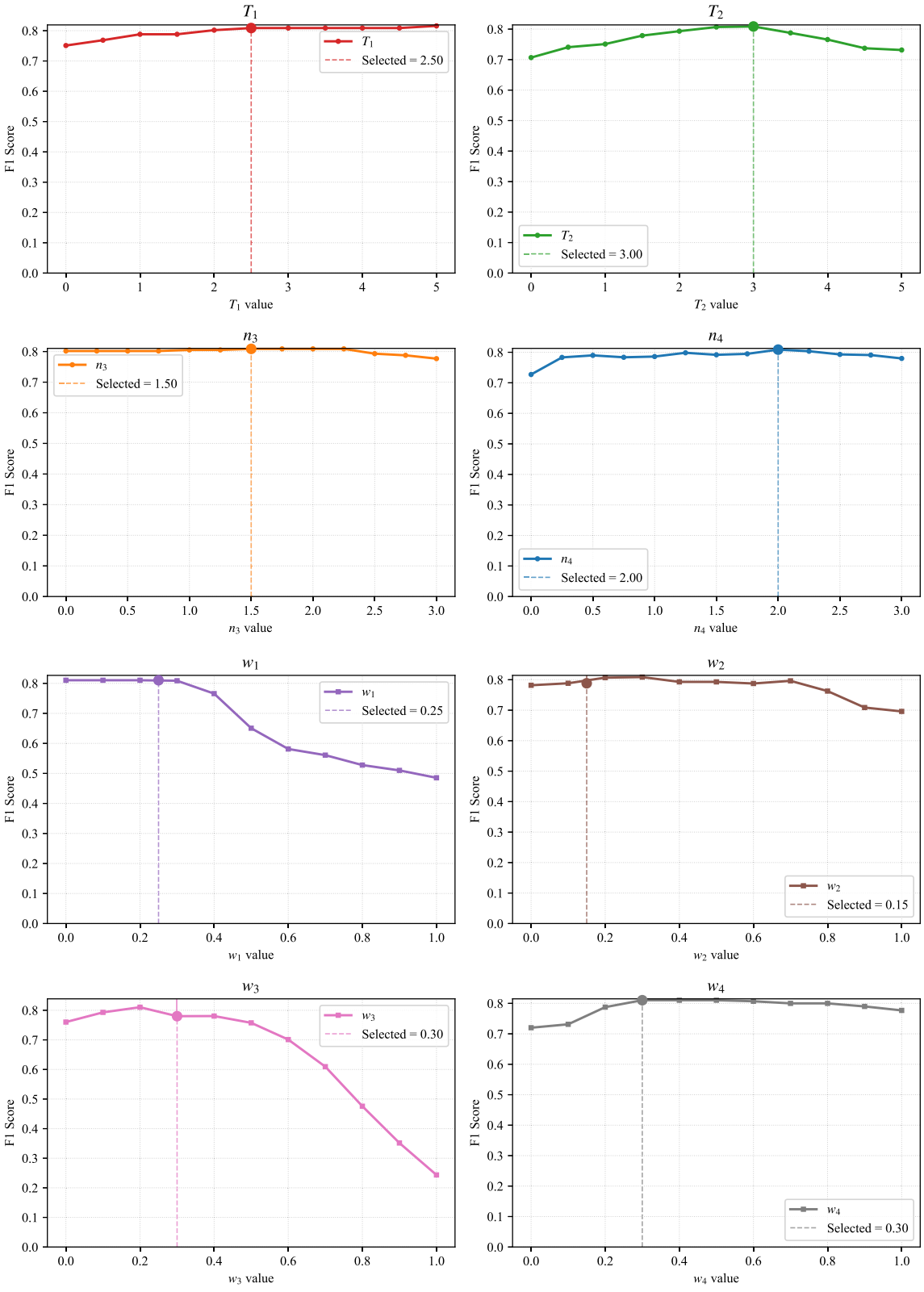

Fig. 15. Results of sensitivity change analysis for each parameter.

6. Conclusion

This paper proposes a Dynamic Context-Adaptive Fusion algorithm for Himawari-8/9 10-minute wildfire detection for immediate Remote Sensing. By combining dynamic contextual statistics, probabilistic multi-feature fusion, and spatiotemporal consistency constraints, the proposed method significantly improves the robustness of wildfire detection.

Compared with other methods, DCAF achieves good results in 50 wildfire scenario tests and cross-validation with MODIS fire products.

Future work will focus on leveraging deep learning models to further mine multi-band spectral features, replacing manually designed feature extractors with 3D-CNN or ConvLSTM networks.

CRediT authorship contribution statement

Baomo Zhang: Writing – original draft, Validation, Methodology. **Qiang Zhang:** Writing – review & editing, Supervision, Conceptualization. **Zishuo Wang:** Writing – review & editing, Visualization, Resources. **Tongde Yang:** Writing – review & editing, Validation, Software.

Declaration of competing interest

The authors declare that they have no known competing financial interests or personal relationships that could have appeared to influence the work reported in this paper.

Acknowledgements

This study is supported in part by the National Natural Science Foundation of China under Grant 62401095; and in part by the Natural Science Foundation of Inner Mongolia Autonomous Region under Grant 2025ZDLH007; and in part by the Dalian Science and Technology Talent Innovation Supporting Project under Grant 2024RQ028; and in part by the China Postdoctoral Science Foundation under Grant 2023M740460 and 2025T180065; and in part by the Natural Science Foundation of Liaoning Province under Grant 2025-BS-0236; and in part by the Fundamental Research Funds for the Central Universities under Grant 3132026239.

Data availability

Data will be made available upon request.

References

Bessho, K., Date, K., Hayashi, M., Ikeda, A., Imai, T., Inoue, H., Kumagai, Y., Miyakawa, T., Murata, H., Ohno, T., 2016. An introduction to Himawari-8/9—Japan's new-generation geostationary meteorological satellites. Journal of the Meteorological Society of Japan. Ser. II 94 (2), 151–183.

Bishop, C.M., 2006. Pattern Recognition and Machine Learning. Springer New York.

Chen, J., Zheng, W., Liu, C., 2017. Application of grassland fire monitoring based on Himawari-8 geostationary meteorological satellite data. J. Nat. Disasters 26, 197–204.

Chen, J., Zheng, W., Liu, C., Tang, S., 2021. Temporal sequence method for fire spot detection using Himawari-8 geostationary meteorological satellite. Natl. Remote Sens. Bull 25, 2095–2102.

Chen, J., Li, R., Tao, M., Wang, L., Lin, C., Wang, J., Wang, L., Wang, Y., Chen, L., 2022a. Overview of the performance of satellite fire products in China: uncertainties and challenges. Atmos. Environ. 268, 118838.

Chen, J., Zheng, W., Wu, S., Liu, C., Yan, H., 2022b. Fire monitoring algorithm and its application on the geo-Kompsat-2A geostationary meteorological satellite. Remote Sens. 14 (11), 2655.

Chen, J., Lv, Q., Wu, S., Zeng, Y., Li, M., Chen, Z., Zhou, E., Zheng, W., Liu, C., Chen, X., Yang, J., Gao, B., 2023. An adapted hourly Himawari-8 fire product for China: principle, methodology and verification. Earth Syst. Sci. Data 15 (5), 1911–1931.

Chowdhury, E.H., Hassan, Q.K., 2015. Operational perspective of remote sensing-based forest fire danger forecasting systems. ISPRS J. Photogramm. Remote Sens. 104, 224–236.

De Almeida Pereira, G.H., Fusioka, A.M., Nassu, B.T., Minetto, R., 2021. Active fire detection in Landsat-8 imagery: a large-scale dataset and a deep-learning study. ISPRS J. Photogramm. Remote Sens. 178, 171–186.

Ding, C., Zhang, X., Chen, J., Ma, S., Lu, Y., Han, W., 2022. Wildfire detection through deep learning based on Himawari-8 satellites platform. Int. J. Remote Sens. 43 (13), 5040–5058.

Filizzola, C., Corrado, R., Marchese, F., Mazzeo, G., Paciello, R., Pergola, N., Tramutoli, V., 2016. RST-FIRES, an exportable algorithm for early-fire detection and monitoring: description, implementation, and field validation in the case of the MSG-SEVIRI sensor. Remote Sens. Environ. 186, 196–216.

Flasse, S., Ceccato, P., 1996. A contextual algorithm for AVHRR fire detection. Int. J. Remote Sens. 17 (2), 419–424.

Friedl, M.A., Sulla-Menashe, D., Tan, B., Schneider, A., Ramankutty, N., Sibley, A., Huang, X., 2010. MODIS collection 5 global land cover: algorithm refinements and characterization of new datasets. Remote Sens. Environ. 114 (1), 168–182.

Giglio, L., Descloitres, J., Justice, C.O., Kaufman, Y.J., 2003. An enhanced contextual fire detection algorithm for MODIS. Remote Sens. Environ. 87 (2–3), 273–282.

Giglio, L., Schroeder, W., Justice, C.O., 2016. The collection 6 MODIS active fire detection algorithm and fire products. Remote Sens. Environ. 178, 31–41.

Gong, A., Li, J., Chen, Y., 2021. A spatio-temporal brightness temperature prediction method for forest fire detection with modis data: a case study in San Diego. Remote Sens. 13 (15), 2900.

Hong, Z., Tang, Z., Pan, H., Zhang, Y., Zheng, Z., Zhou, R., Ma, Z., Zhang, Y., Han, Y., Wang, J., 2022. Active fire detection using a novel convolutional neural network based on Himawari-8 satellite images. Front. Environ. Sci. 10, 794028.

Hong, Z., Tang, Z., Pan, H., Zhang, Y., Zheng, Z., Zhou, R., Zhang, Y., Han, Y., Wang, J., Yang, S., 2023. Near real-time monitoring of fire spots using a novel SBT-FireNet based on Himawari-8 satellite images. IEEE J. Sel. Top. Appl. Earth Obs. Remote Sens. 17, 1719–1733.

Johnston, J.M., Johnston, L.M., Wooster, M.J., Brookes, A., McFayden, C., Cantin, A.S., 2018. Satellite detection limitations of sub-canopy smouldering wildfires in the North American boreal forest. Fire 1 (2), 28.

Justice, C., Giglio, L., Korontzi, S., Owens, J., Morisette, J., Roy, D., Descloitres, J., Alleaume, S., Petitcolin, F., Kaufman, Y., 2002. The MODIS fire products. Remote Sens. Environ. 83 (1–2), 244–262.

Kennedy, P., Belward, A., Gregoire, J., 1994. An improved approach to fire monitoring in West Africa usingavhrr data. Int. J. Remote Sens. 15 (11), 2235–2255.

Laneve, G., Castronuovo, M.M., Cadau, E.G., 2006. Continuous monitoring of forest fires in the Mediterranean area using MSG. IEEE Trans. Geosci. Remote Sens. 44 (10), 2761–2768.

Liew, S.C., 2019. Detecting active fires with Himawari-8 geostationary satellite data. In: IGARSS 2019-2019 IEEE International Geoscience and Remote Sensing Symposium, pp. 9984–9987.

Liu, C., Chen, R., He, B., 2023. Integrating machine learning and a spatial contextual algorithm to detect wildfire from Himawari-8 data in southwest China. Forests 14 (5), 919.

Liu, Z., Zhang, Q., Zhang, B., Zhu, J., 2026. Validation of Himawari-8/9 10-minute wildfire products: comparisons with MODIS and VIIRS from 2015 to 2023. Remote Sens. Appl. Soc. Environ. 101868.

Maier, S.W., Russell-Smith, J., Edwards, A.C., Yates, C., 2013. Sensitivity of the MODIS fire detection algorithm (MOD14) in the savanna region of the Northern Territory, Australia. ISPRS J. Photogramm. Remote Sens. 76, 11–16.

Moritz, M.A., Batllori, E., Bradstock, R.A., Gill, A.M., Handmer, J., Hessburg, P.F., Leonard, J., McCaffrey, S., Odion, D.C., Schoennagel, T., 2014. Learning to coexist with wildfire. Nature 515 (7525), 58–66.

Parto, F., Saradjian, M., Homayouni, S., 2020. MODIS brightness temperature change-based forest fire monitoring. J. Indian Soc. Remote Sens. 48 (1), 163–169.

Schroeder, W., Csiszar, I., Giglio, L., Ellicott, E., Justice, C., 2011. Satellite active fire product validation using high spatial resolution reference data. In: 34th International Symposium on Remote Sensing of Environment-the GEOSS Era: Towards Operational Environmental Monitoring.

Schroeder, W., Oliva, P., Giglio, L., Csiszar, I.A., 2014. The new VIIRS 375 m active fire detection data product: algorithm description and initial assessment. Remote Sens. Environ. 143, 85–96.

Seydi, S.T., Saeidi, V., Kalantar, B., Ueda, N., Halin, A.A., 2022. Fire-net: a deep learning framework for active forest fire detection. J. Sens. 2022 (1), 8044390.

Wang, Q., Zhang, Q., Yang, T., Sun, W., Yuan, Q., 2026. SGD-SST 2.0: seamless global daily sea surface temperature products cross-sensors generating from 2003 to 2025. Expert Syst. Appl. 132259.

Wickramasinghe, C.H., Jones, S., Reinke, K., Wallace, L., 2016. Development of a multi-spatial resolution approach to the surveillance of active fire lines using Himawari-8. Remote Sens. 8 (11), 932.

Xie, Z., Song, W., Ba, R., Li, X., Xia, L., 2018. A spatiotemporal contextual model for forest fire detection using Himawari-8 satellite data. Remote Sens. 10 (12), 1992.

Xu, W., Wooster, M.J., 2023. Sentinel-3 SLSTR active fire (AF) detection and FRP day-time product-algorithm description and global intercomparison to MODIS, VIIRS and landsat AF data. Sci. Remote Sens. 7, 100087.

Xu, G., Zhong, X., 2017. Real-time wildfire detection and tracking in Australia using geostationary satellite: Himawari-8. Remote Sens. Lett. 8 (11), 1052–1061.

Yan, J., Qu, J., Ran, M., Zhang, F., 2020. Himawari-8 AHI fire detection in clear sky based on time-phase change. J. Remote Sens. 24 (5), 571–577.

Zhang, Q., Yuan, Q., Song, M., Yu, H., Zhang, L., 2022. Cooperated spectral low-rankness prior and deep spatial prior for HSI unsupervised denoising. IEEE Trans. Image Process. 31, 6356–6368.

Zhang, D., Huang, C., Gu, J., Hou, J., Zhang, Y., Han, W., Dou, P., Feng, Y., 2023a. Real-time wildfire detection algorithm based on VIIRS fire product and Himawari-8 data. Remote Sens. 15 (6), 1541.

Zhang, H., Sun, L., Zheng, C., Ge, S., Chen, J., Li, J., 2023b. A weighted contextual active fire detection algorithm based on Himawari-8 data. Int. J. Remote Sens. 44 (7), 2400–2427.

Zhang, Q., Zhu, J., Huang, Y., Yuan, Q., Zhang, L., 2023c. Beyond being wise after the event: combining spatial, temporal and spectral information for Himawari-8 early-stage wildfire detection. Int. J. Appl. Earth Obs. Geoinf. 124, 103506.

Zhang, Q., Dong, Y., Zheng, Y., Yu, H., Song, M., Zhang, L., Yuan, Q., 2024a. Three-dimension spatial–spectral attention transformer for hyperspectral image denoising. IEEE Trans. Geosci. Remote Sens. 62, 1–13.

Zhang, Q., Zheng, Y., Yuan, Q., Song, M., Yu, H., Xiao, Y., 2024b. Hyperspectral image denoising: from model-driven, data-driven, to model-data-driven. IEEE Trans. Neural Netw. Learn. Syst. 35 (10), 13143–13163.

Zhang, Q., Zhang, X., Xiao, Y., Xie, H., 2025a. Deep low-rank tensor embedded network for hyperspectral image super-resolution. Expert Syst. Appl. 129864.

Zhang, Q., Zheng, Y., Dong, Y., Yu, C., Yuan, Q., 2025b. Hyperspectral image mixed noised removal via jointly spatial and spectral difference constraint with low-rank tensor factorization. Eng. Appl. Artif. Intell. 149, 110508.

Zhang, Q., Zhu, J., Dong, Y., Zhao, E., Song, M., Yuan, Q., 2025c. 10-minute forest early wildfire detection: fusing multi-type and multi-source information via recursive transformer. Neurocomputing 616, 128963.
Zhang, B., Zhang, Q., Gao, W., Liu, B., Wen, J., 2026a. 10-minute level and near real-time wildfire detection: integrating multiple features for himawari-8/9 satellite. Int. J. Remote Sens. 1–25.
Zhang, Q., Gao, W., Sun, W., Dong, Y., Zheng, Y., 2026b. Ssgmrn: spatial-spectral global modeling retentive network for hyperspectral image denoising. Optics and Laser Technology 202, 115381.
Zheng, Z., Hu, H., Huang, W., Zhou, F., Ma, Y., Liu, Q., Jiang, L., Wang, S., 2024. Wildfire detection based on the spatiotemporal and spectral features of Himawari-8 data. IEEE Trans. Geosci. Remote Sens. 62, 1–13.